

# Benchmark Aerostructural Models for the Study of Transonic Aircraft Wings

Timothy R. Brooks,\* Gaetan K. W. Kenway,† and Joaquim R. R. A. Martins‡  
*University of Michigan, Ann Arbor, Michigan 48105*

DOI: 10.2514/1.J056603

Since its introduction, the NASA Common Research Model has proved a useful aerodynamic benchmark for predicting computational-fluid-dynamics-based drag and aerodynamic design optimization. The model was originally conceived as a purely aerodynamic benchmark, and as such the wing geometry corresponds to the deflected shape at its nominal 1g flight condition. However, interest has been growing to extend this model to aeroelastic studies. Unfortunately, because of its predefined deflection, the model is not suitable for aeroelastic analysis and design. To address this issue, an undeflected Common Research Model is defined through an inverse design procedure that includes the outer mold line geometry of the undeflected wing and the corresponding internal wingbox structure. Additionally, because modern transport aircraft are trending toward higher-aspect-ratio wing designs, a higher-aspect-ratio variant of the Common Research Model wing is developed to assess next-generation wing designs. This variant has an aspect ratio of 13.5 and is designed by using buffet-constrained multipoint aerostructural optimization. The purpose of these models is to provide publicly available benchmarks for aeroelastic wing analysis and design optimization.

## Nomenclature

$C_{M_y}$	=	pitching moment coefficient
$C_p$	=	coefficient of pressure
$c$	=	engine thrust specific fuel consumption
$D, C_D$	=	drag, drag coefficient
$F$	=	wingbox finite element method external load vector
$K$	=	wingbox finite element method stiffness matrix
$L, C_L$	=	lift, lift coefficient
LGW	=	landing weight
$M$	=	Mach number
$R$	=	aircraft range
$T_i$	=	multipoint fuel burn weighting
$t/c$	=	thickness-to-chord ratio
$u$	=	wingbox finite element method nodal displacement
$V$	=	wingbox volume
$V_\infty$	=	aircraft flight speed
$V_{\text{fuel}}$	=	fuel volume
$\alpha$	=	angle of attack

## I. Introduction

MODERN Reynolds-averaged Navier–Stokes (RANS) computational fluid dynamics (CFD) solvers feature a variety of turbulence models and parameters that differ from solver to solver. These modeling differences result in small solution differences for the same geometry and flight condition, depending on which solver is used. To validate and compare different CFD solvers, a number of benchmark geometries have been developed, including the ONERA

M6 wing [1], the German Aerospace Research Center DLR-F4 [2], and the NASA Common Research Model (CRM) [3]. The CRM was developed to be representative of a long-range twin-aisle transport aircraft configuration and has been used in the AIAA Drag Prediction Workshop since 2008 [3]. The CRM geometry features a fuselage, wing, horizontal tail, engine nacelle, and pylon.

Because the CRM was originally developed for validating various CFD tools, the wing geometry was designed to match the deflected wing shape under the nominal 1g cruise condition. This is ideal from the viewpoint of aerodynamic analysis because it eliminates the need to find the aeroelastically deformed shape. For single-point aerodynamic shape optimization, a single flying shape is also acceptable, but such optimizations do not yield practical results because the resulting performance is not robust with respect to changes in flight conditions. However, when optimizing aerodynamic shape while considering multiple flight conditions, the use of a single rigid shape is no longer appropriate because different flight conditions yield different wing shapes. Thus, even for a purely aerodynamic analysis, aeroelastic effects need to be considered. As an example, Keye et al. [4] showed that significant aeroelastic deformations were experienced in a wind-tunnel test of the CRM. Furthermore, they showed that, to accurately predict the drag polar, these aeroelastic deformations must be accounted for in the CFD analysis.

Despite the challenges mentioned previously, a series of aerodynamic shape optimization cases based on the 1g deflected shape of the CRM wing have been considered for the Aerodynamic Design Optimization Discussion Group benchmarks [5–11]. Many of these works found that single-design-point aerodynamic optimization leads to results with poor off-design performance and that multiple flight conditions must be considered to lead to a practical and robust design [5,8]. More recently, several optimization cases featuring multiple design conditions were also defined and solved [7,12]. These benchmark cases have been successful in getting practitioners from academia and industry to solve the same problem. Herein, we aim to leverage the efforts invested into the validation, verification, and design optimization of the CRM wing by developing aerostructural benchmarks based on the undeflected Common Research Model (uCRM).

Although numerical optimization offers promising results for aerodynamic wing design, it is not without drawbacks. To capture the inherent coupling between the structural response and the aerodynamics of the wing under various flight conditions, a multidisciplinary design optimization (MDO) approach and aerolastic model are required. Interest has been growing in using the CRM configuration as a model for aerostructural (static aeroelastic) as well as aeroelastic and aeroservoelastic analysis and design. The transonic conditions for which the CRM was designed makes it an ideal model for an aeroelastic

Presented as Paper 2017-4456 at the AIAA Aviation Forum and Exposition 2017, Denver, CO, 5–9 June 2017; received 5 September 2017; revision received 7 February 2018; accepted for publication 26 February 2018; published online Open Access 31 May 2018. Copyright © 2018 by the authors. Published by the American Institute of Aeronautics and Astronautics, Inc., with permission. All requests for copying and permission to reprint should be submitted to CCC at [www.copyright.com](http://www.copyright.com); employ the ISSN 0001-1452 (print) or 1533-385X (online) to initiate your request. See also AIAA Rights and Permissions [www.aiaa.org/randp](http://www.aiaa.org/randp).

\*Ph.D. Candidate, Department of Aerospace Engineering. Student Member AIAA.

†Research Investigator, Department of Aerospace Engineering; currently Science and Technology Corporation, Moffet Field, California 94035. Senior Member AIAA.

‡Professor, Department of Aerospace Engineering. Associate Fellow AIAA.

benchmark. A number of aeroelastic studies featuring optimization based on the CRM geometry have been conducted by using panel methods [13,14]. This includes the work of Klimmek [15], who developed an aeroelastic model for the CRM that uses an inverse design optimization to recover the jig geometry. This model was later used in a RANS-based aerostructural design optimization study conducted by Keye et al. [16]. Although low-fidelity models incur a lower computational cost and are widely used in industry for preliminary design, the optimization tends to exploit the physics missing from such models, and so a conservative approach is required. One example of missing physics was pointed out by Lyu et al. [17], who noted that, for an Euler-based aerodynamic optimization, the design converged to a shape different from that obtained with RANS-based optimization. Furthermore, when the shape obtained with the Euler optimization was analyzed by using a RANS-based solver, the performance was worse than the initial design due to shock-induced separation effects that the Euler model missed.

A number of efforts have already used higher-fidelity static aerostructural optimization that features RANS-based CFD solvers coupled with a finite element method (FEM) solver using the model with aspect ratio (AR) 9 that we develop in this work (uCRM-9) [18,19]. Because of a continual push for increased aircraft efficiency and reduction in fuel burn, interest has also been growing in developing high-AR wings without a disproportionate weight penalty through the use of future technologies such as tow-steered composites [20,21], morphing trailing-edge wings [22], and additive manufactured wingbox topologies [23]. Each of these studies used the 13.5 AR model developed in this work (uCRM-13.5).

Although these studies produced markedly more robust results than single-point design, they neglected buffet, which is a critical consideration in transonic wing design. In the transonic flight regime, shocks may occur over the upper surface of the wing during cruise flight. These shocks increase in strength with both lift coefficient and Mach number. Shocks can lead to strong interactions between oscillations in the shock position and shock-induced flow separation, causing an unsteady aerodynamic instability known as transonic buffet. This phenomenon is undesirable because it results in intense structural vibration and may lead to loss of aircraft control. To ensure a safe aircraft, regulations require a sufficient margin between buffet onset and the nominal operating cruise envelope to ensure the ability to maneuver at an increased lift without experiencing buffet.

Because buffet is inherently an unsteady phenomenon, accurately modeling it generally requires expensive unsteady aerodynamic simulations. Recently, Kenway and Martins [24] developed a formulation to constrain buffet onset in design optimization by using a separation-based prediction metric based on steady CFD. They found that buffet onset could be correlated with the amount of separated flow on the upper surface of the wing and that, for the CRM, buffet onset occurs when this separated flow area reaches 4% of the wing reference area. After validating the prediction metric for the CRM, they compared the design optimizations done with and without the constraint. They concluded that, when the constraint was not enforced, the aircraft did not have the required margin at the flight conditions for peak performance, and so the aircraft would have to fly at suboptimal Mach and lift coefficient to satisfy the buffet onset margin. However, the designs obtained while enforcing the buffet onset constraint led to peak performance right at the buffet onset boundary. Thus, the buffet onset constraint must be enforced to obtain a practical wing design through optimization. For this reason, we use the same approach in the present work to predict and constrain buffet onset when defining our aerostructural models.

Because of the growing interest in aerostructural analysis and optimization via the CRM and future high-AR wing designs, the goal of the present work is to develop two aerostructural benchmark geometries: an AR 9 wing based on the CRM (uCRM-9), and a higher-AR variant (uCRM-13.5). Because these models are used for aerostructural analyses, the 1g “built-in” deflections become problematic, and we must instead define the jig (undeflected) shape. The goal is for these models to provide a useful benchmark for aeroelastic studies. Toward this end, all files associated with these

designs—both geometry and mesh files—are made publicly available.<sup>§</sup> The details of the files provided are included in the Appendix.

This paper is structured as follows. We first describe the computational tools used to perform the multidisciplinary analysis and optimization required to define both aerostructural models, following which we describe the procedure used to define the uCRM-9 geometry and the structural wingbox model. Next, we describe the steps used to transform the planform of the uCRM-9 model into its higher-AR variant, the uCRM-13.5. Finally, we describe the buffet-constrained multipoint aerostructural optimization used to finalize the definition of the uCRM-13.5 wing geometry and structure, and then end with concluding remarks on the models.

## II. Computational Framework

An accurate assessment of the aeroelastic performance of flexible-wing designs, such as the CRM geometry, requires a framework featuring a tightly coupled high-fidelity aerodynamic and structural mechanics solver. Toward this end, the work reported herein was conducted by using the MDO for Aircraft Configurations with High fidelity (MACH) framework [25], whose components are briefly described in the remainder of this section. Kennedy and Martins [26] and Kenway et al. [25] provide more detailed descriptions.

For the purposes of high-fidelity aeroelastic analysis, this framework is composed of both a RANS-based CFD solver and a structural finite element solver. The two solvers are coupled by a CFD mesh movement algorithm, which is used to propagate the structural deflections of the wing to the CFD volume mesh. The framework also allows for variations in wing geometry by using a shape parametrization algorithm that allows for changes in both the aerodynamic and structural shape of the wing during the optimization. Finally, a gradient-based optimizer uses the aerostructural derivatives computed by using a coupled adjoint approach to solve the optimization problem. The MACH framework has proven effective in a number of aerostructural design optimization studies [21,22,27,28].

### A. Aerodynamic Solver

A high-fidelity CFD solver is required for capturing the full physics of the aerodynamics. In the MACH framework, we use ADflow [17], which is a second-order finite volume CFD solver. ADflow solves the steady RANS equations on structured multiblock and overset meshes. A single-equation Spalart–Allmaras turbulence model is considered in this work. ADflow is used to compute the aerodynamic forces, such as lift, drag, and pitching moment. By using a discrete adjoint implementation developed by Mader et al. [29] and Lyu et al. [17] via automatic differentiation (AD), ADflow efficiently computes the derivatives of the aerodynamic functions of interest with respect to large numbers of design variables.

### B. Structural Solver

To accurately compute the aeroelastic deflection of the wing, a high-fidelity structural solver is also required. The structural solver used in the MACH framework is the Toolkit for Analysis of Composite Structures (TACS) [30]. TACS is a FEM solver that is specifically designed for solving structures consisting of thin shell components, which are typical in aerospace structures. The solver uses a parallel direct factorization method, which allows it to efficiently and accurately solve the poorly conditioned structural problems that are inherent in thin shell structures. In addition to computing the structural displacements, TACS computes other structural functions of interest, such as material failure and buckling loads. Like its aerodynamic counterpart, TACS features an efficient adjoint method for computing structural sensitivities.

<sup>§</sup>Data available online at <http://mdolab.engin.umich.edu/ucrm> [retrieved 7 May 2018].

### C. Mesh Movement

A mesh movement algorithm is required for aerostructural analysis and to apply changes in geometric shape during optimization. The purpose of mesh movement is to deform the CFD volume mesh given displacements in the surface geometry. This procedure takes the changes to the surface mesh and propagates them through the volume of the CFD mesh. The mesh movement algorithm used in MACH is an inverse distance weighting method, similar to that described by Uyttersprot [31]. This method has the benefit of preserving the mesh quality near surfaces, which is necessary for accurately capturing the boundary-layer physics.

### D. Aerostructural Solver

To solve aerostructural problems, a coupling scheme is required between the structural and aerodynamic solvers. In MACH, this coupling is accomplished through a block Gauss–Seidel scheme. First, the tractions due to the aerodynamic loads are determined by using ADflow. These loads are then applied to the TACS FEM from which the displacements of the wing can be calculated along with structural functions of interest, such as buckling and material failure. The structural displacements are then transferred to the nodes on the surface of the wing in the CFD mesh by using a system of rigid links, as proposed by Brown [32]. The displacements at the surface nodes are then extrapolated to the rest of the nodes throughout the CFD volume mesh by using the mesh movement algorithm mentioned previously. The aerodynamics is solved again for the new mesh, and the process is repeated until convergence. As with the previous solvers, the aerostructural solver is capable of assembling the coupled adjoint from the adjoint of the structural and aerodynamic disciplines to evaluate the coupled aerostructural derivatives required to solve the design optimization problem [25]. This approach computes the cross-disciplinary sensitivities inherent to flexible wing design in an accurate and efficient manner, enabling gradient-based optimization with  $\mathcal{O}(10^3)$  design variables.

### E. Geometric Parameterization

For the optimization, the wing shape and planform are parametrized through a free-form deformation (FFD) volume. The implementation is that of Kenway and Martins [27]. The surface of the wing is embedded in a volume with control points distributed over the volume surface. As the control points move, the shape inside the volume deforms in a continuous manner, giving the optimizer control over the cross-sectional shape, twist, and planform (sweep and span) of the wing. There is an additional smaller sub-FFD that encloses the horizontal stabilizer, which allows its incidence to be controlled to trim the aircraft. An example of the FFD model used for this work is shown in Fig. 1. A total of 240 control points are distributed on the surface of this FFD volume to parameterize the wing geometry.

### F. Optimizer

Aerostructural design problems typically feature a large sparse constraint Jacobian. Therefore, it is desirable to use an optimizer that takes advantage of the sparse nature of the problem. For this reason,

all optimization problems discussed herein are solved by using SNOPT (from “Sparse Nonlinear Optimizer”) [33], a quasi-Newton gradient-based optimizer that works well for optimization problems featuring a large number of sparse nonlinear constraints. The optimization tool is wrapped with the Python interface pyOpt [34].

## III. uCRM-9 Definition

For both the uCRM-9 and the uCRM-13.5, we only model the structure of the wingbox. Although structural models for the wingbox of the CRM are available from the CRM website,<sup>†</sup> these models are based on the 1g flight shape of the wing. For this reason, we design an undeflected jig shape and structural model for the wing. We design the uCRM-9 model with a jig shape and structure that deforms into the shape of the original outer mold line (OML) of the CRM model at a nominal cruise condition ( $M = 0.85$ ,  $C_L = 0.5$  at 37,000 ft) [35].

The procedure used to accomplish this can be summarized as follows. First, we define a wingbox layout based on a similar aircraft and size the structure by using representative aerodynamic loads. Next, we apply an inverse design procedure that iteratively removes the deflection from the OML and wingbox geometry and update the structural sizing to ensure that the aeroelastically deflected shape matches the nominal deflection profile of the CRM. This is similar to the design procedure used by Kenway et al. [18], although with a few key differences. In the original work, the stiffeners were not modeled in the wingbox structural model, whereas we model them herein by using a smeared-stiffness approach. In addition, when we size the wingbox, we enforce buckling constraints for all the maneuver loads, whereas the previous work only considered material failure. Finally, the aerodynamic model used in this work uses a finer mesh and includes the horizontal stabilizer in the geometry. In the remainder of this section, we describe this procedure in more detail.

### A. Wingbox Structural Definition

As the first step of the uCRM-9 design process, we define a realistic wingbox layout. Because of the proprietary nature of internal wing structures, no publicly available data are available on wingboxes for modern transport aircraft. We thus based our layout on publicly available cutaway drawings of the Boeing 777-200ER aircraft<sup>\*\*</sup> because this aircraft is the most similar to the CRM in terms of size and performance. Figure 2 shows the planform view of the 777-200ER extracted from the aircraft planning document [36] superimposed over a best guess of the wingbox outline (left) and the CRM planform with our wingbox layout (right). By using digital versions of the Boeing 777 drawing, we estimated the extent of the wingbox at the root and tip. We then rounded off the measurements to obtain the percentage locations with respect to the local chord listed in Table 1. This information was sufficient to define the wingbox structure planform for the CRM geometry. We generated the wingbox for the CRM by using the same proportions (front and rear spar location, rib spacing, etc.) and structural layout of the Boeing 777 wingbox. Because of differences in sweep and span, we could not use the Boeing 777 wingbox layout directly in the CRM planform.

The CRM wingbox is composed of an upper and lower skin, two spars, 49 ribs, and an engine mount panel. The leading-edge spar is straight, except for a kink at the wing–body junction, whereas the trailing-edge spar features an additional kink at the Yehudi break. The center wingbox section includes four ribs oriented parallel to the fuselage, with the remaining 45 ribs distributed along the span of the wing perpendicular to the leading edge, with the exception of the closeout rib at the tip. We include an additional panel between two ribs at the Yehudi break. This panel is used to mount the engine to the wing, along with the leading-edge spar at this location. The structural model also includes external nonstructural masses. The masses include discrete leading- and trailing-edge lumped masses (Fig. 2), which are used to model the effect of the mounted actuators and

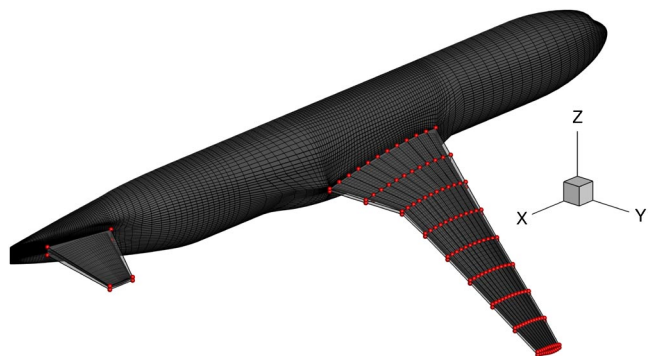


Fig. 1 FFD volume and control points (red spheres) used for this work.

<sup>†</sup>Data available online at <https://commonresearchmodel.larc.nasa.gov/fem-file> [retrieved 6 May 2018].

<sup>\*\*</sup>Data available online at <http://www.flightglobalimages.com/boeing-777-200-cutaway-drawing/print/1577243.html> [retrieved 14 December 2017].



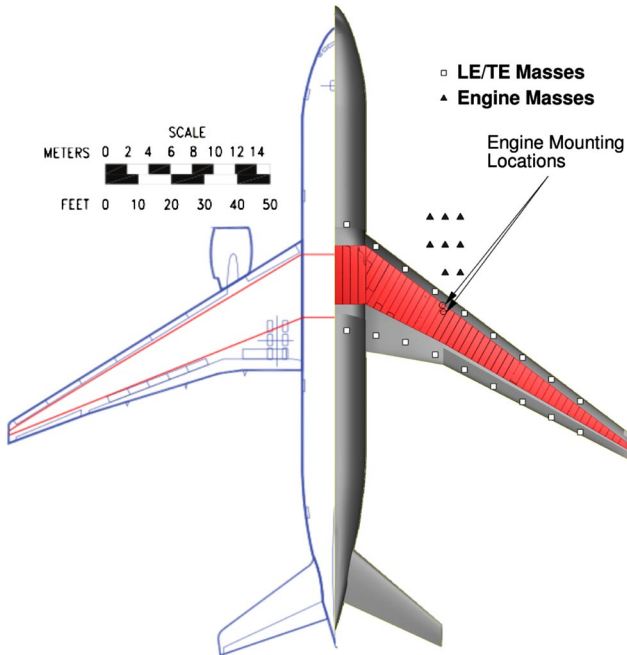


Fig. 2 Boeing 777 (left) and uCRM-9 (right). The CRM has a slightly lower wing area and span, and more sweep than the Boeing 777.

control surfaces. These masses are attached at spanwise locations along either spar. Finally, we also include the inertial effects of the engine and the fuel weight present in the fuel bays of the wingbox by adding the appropriate masses.

Figure 3 illustrates the boundary conditions used to link the wingbox structural FEM to the fuselage geometry. The innermost wingbox rib is clamped at the symmetry plane, and so all the displacements and rotations for the elements in that rib are fixed to zero. In addition, the rib at the wing-fuselage junction is constrained such that the vertical and longitudinal displacements are fixed. Thus, small displacements in the spanwise direction and rotation are permitted, allowing for some bending deformation in this region. However, these displacements are very small in practice.

Once we defined the planform of the wingbox, we used an in-house tool to generate the geometry of the wingbox and its components, conforming with the wing OML. Figure 4 shows the final wingbox for the CRM. We used the commercial grid-generation tool ICEMCFD to generate surface meshes for the wingbox geometry. The FEM mesh used for this model consists of 10,285 shell elements with a total of 156,826 degrees of freedom (DOFs). This initial wingbox provides an initial guess for the structure of the wing jig shape. However, because this first guess is based on the CRM OML, it also features the built-in 1g deflection in its geometry. We remove this deflection in the subsequent inverse design procedure, so that the CRM wing geometry can be recovered from the jig through structural deflection of the wingbox.

## B. Aerodynamic Loads

We use a fixed aerodynamic load distribution to recover the undeflected wing shape. This aerodynamic load distribution was computed by using RANS CFD for the CRM wing-body-tail configuration at its nominal cruise condition with meshes from the

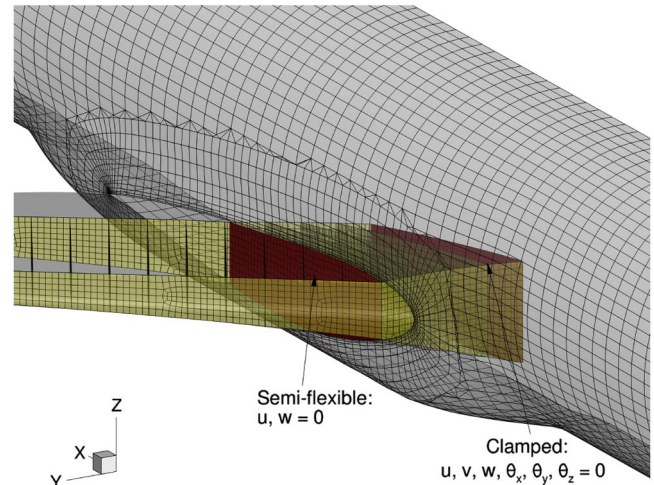


Fig. 3 The wingbox structure is clamped at the symmetry plane and partially constrained at the wing-fuselage junction.

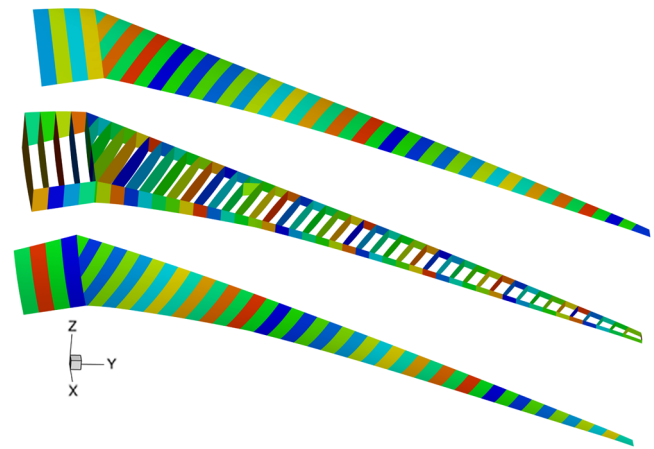


Fig. 4 uCRM-9 wingbox layout: each colored panel represents a patch independently sized by the optimizer.

Fourth Drag Prediction Workshop, but with a flight Reynolds number matching the full-scale aircraft, as opposed to wind-tunnel conditions. The CFD grid used for this model was an overset mesh consisting of 9.82 million volume cells. Figure 5 shows the CRM mesh and  $C_p$  distribution for the nominal flight conditions. We then store the converged aerodynamic pressure and skin-friction forces as tractions (force per unit area). For the inverse design procedures, we only apply these tractions to the wingbox because the other components of the design are assumed to be rigid.

## C. Sizing of Structural Model

Once we fix the aerodynamic loads, the wingbox components are sized through numerical optimization. All components in the wingbox structure are modeled by using aluminum 7000 series alloy, whose properties are listed in Table 2.

Like all modern transport aircraft, our wingbox uses blade-stiffened panels for the skins, ribs, and spars. The stiffeners are not included explicitly in the FEM model of the wingbox. Instead, we model the effect of their stiffness by homogenizing (smearing) them into the stiffness of the wingbox panels. Kennedy et al. [37] describe the smeared-stiffness approach in more detail. By using this approach, we can analyze the panel-level buckling while considering multiple buckling modes. These buckling modes include intra-stiffener skin buckling, stiffener buckling, and coupled stiffener-skin buckling modes. All three buckling modes are aggregated into a single scalar value by using a Kreisselmeier-Steinhauser (KS) function [38,39], which yields a conservative approximation of the most violated case.

Table 1 Spar positions (in percent chord) for the Boeing 777 and uCRM-9 wingbox

Spar location	777 estimated, %	uCRM-9, %
Leading-edge spar root	10.4	10
Leading-edge spar tip	36.1	35
Trailing-edge spar root	59.6	60
Trailing-edge spar tip	60.7	60

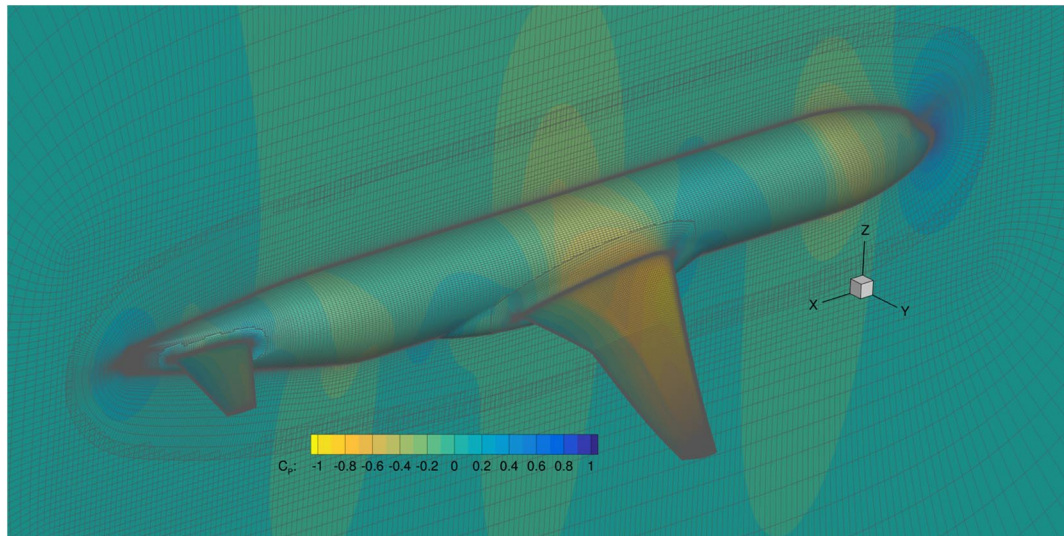


Fig. 5 CRM wing-body-tail CFD solution and mesh used to generate loads.

Structural optimization is used to structurally size the wingbox. The optimization consists of minimizing the mass while enforcing failure and buckling constraints for a 2.5g and a  $-1g$  maneuver load condition. The loads are computed through an intermediate high-fidelity aerostructural analysis and are frozen during the structural optimization procedure. The skin, ribs, and spar panels are constrained from failing or buckling in the preceding load cases by applying a safety factor of 1.5 to the loads. In this structural sizing procedure, we do not include other load cases that are important in practical aircraft design, such as taxi bumps, roll maneuvers, and dynamic gust conditions. However, the load cases considered here suffice for a representative structural model for academic research.

The structural analysis includes inertial load relief from the structure, leading-edge/trailing-edge masses, engine, and fuel. The engine mass corresponds roughly to the mass of a GE90 engine (7500 kg), and the fuel inertial loads can reach up to 55,000 kg of fuel stored in the fuel bays of each half wingbox. The design variables are stiffener pitch (spacing), stiffener height, stiffener thickness, and panel thickness. The stiffener pitch for the upper and lower skins are the same everywhere. The remaining structural variables are free to change (within their bounds) from one panel to the next. Figure 6 shows the panel definition distribution across the primary wing structure.

#### D. Jig Outer Mold Line and Wingbox Inverse Design Procedure

Given the  $1g$  OML of the original CRM, the wingbox structural layout and sizing, and the aerodynamic loads, we determine the jig shapes for the OML and wingbox. This is accomplished by solving a least-squares optimization problem where we minimize the difference between the CRM OML points,  $X_T$ , and points on the displaced jig shape under the nominal  $1g$  loads,  $X_{\text{disp}}$ . The displaced points are found by taking the jig points and adding the structural displacements  $u$  from the applied aerodynamic loads ( $X_{\text{disp}} = X_{\text{jig}} + u$ ). The optimizer changes only the geometry of the wing jig through the FFD  $x$ ,  $y$ , and  $z$  coordinates to match the two sets of points. The goal is to match the two sets of points  $X_T$  and  $X_{\text{disp}}$  such that the flying shape of the CRM wing is achieved through the structural displacement at the nominal flight condition. Once the FFD shape variables are found, we apply them to the initial CRM geometry and wingbox to remove the deflection and achieve a new approximate jig geometry. The new wingbox geometry

is then structurally resized by using another structural optimization. The procedure is then repeated until the subsequent geometry changes are deemed to be negligible. This procedure is described in detail in Algorithm 1, where  $K$  and  $F$  are, respectively, the FEM stiffness matrix and external (including aerodynamic and inertial) nodal force vector of the wingbox structure.

At the end of each iteration of the inverse design procedure, the location of the tractions must be updated to reflect their new locations relative to the updated jig geometry. Several outer-loop iterations are required because the generation of the new structural geometry reorients the ribs to be vertical. This is a small correction, but a noticeable change occurs between iterations 1 and 2.

Figure 7 shows the sequence of inverse design results leading to the finalized wing jig. The  $n = 0$  shape represents the original CRM wing geometry. After three outer iterations of the preceding procedure, the changes between successive jig shapes are small. By the final iteration, the objective of the least-squares inverse design optimization only changes by 0.11% in subsequent iterations. The surface for  $n = 3$  is nearly indistinguishable from that for  $n = 2$ , only differing near the tips. The mass of the final structure of the wingbox, including both wings, is 23,916 kg, which is comparable to the mass of 22,988 kg that Klimmek [15] found for the CRM by using a similar procedure, with a panel code for the aerodynamic model. The jig shapes for this OML and corresponding wingbox geometry define uCRM-9.

#### E. Aerostructural Verification

To verify the resulting jig shapes and wingbox sizing, we do an aerostructural analysis of the uCRM-9 and compare it to the aerodynamic analysis of the CRM. Figure 8 compares the upper-surface  $C_p$  contours, spanwise  $C_p$  slices, and aerodynamic coefficients of interest. From these results, we find that the  $C_p$  distributions are in good agreement, although slight differences appear that can be attributed to the 0.04 deg difference in the angle of attack in the aerostructural solution. This difference in angle of attack is necessary to match the lift coefficient of the original CRM case. Despite the difference in angle of attack, the drag coefficients differ by 0.001%, which approaches the aerostructural solver solution tolerance. Finally, by comparing the pitching moment  $C_{M_y}$  of both models, we see a difference of only 4%. From these results, we conclude that the inverse design procedure successfully produces a representative aeroelastic model for the CRM wing.

#### F. Grid Convergence Study

We now study the grid convergence of the uCRM-9 aerostructural model to assess the convergence properties of both the model and the aerostructural solver. This study consists of a coupled aerostructural

Table 2 Wingbox material properties

Parameter	Value
Density	2780 kg/m <sup>3</sup>
Young's modulus	$73.1 \times 10^9$ Pa
Poisson's ratio	0.3
Yield strength	$420 \times 10^6$ Pa

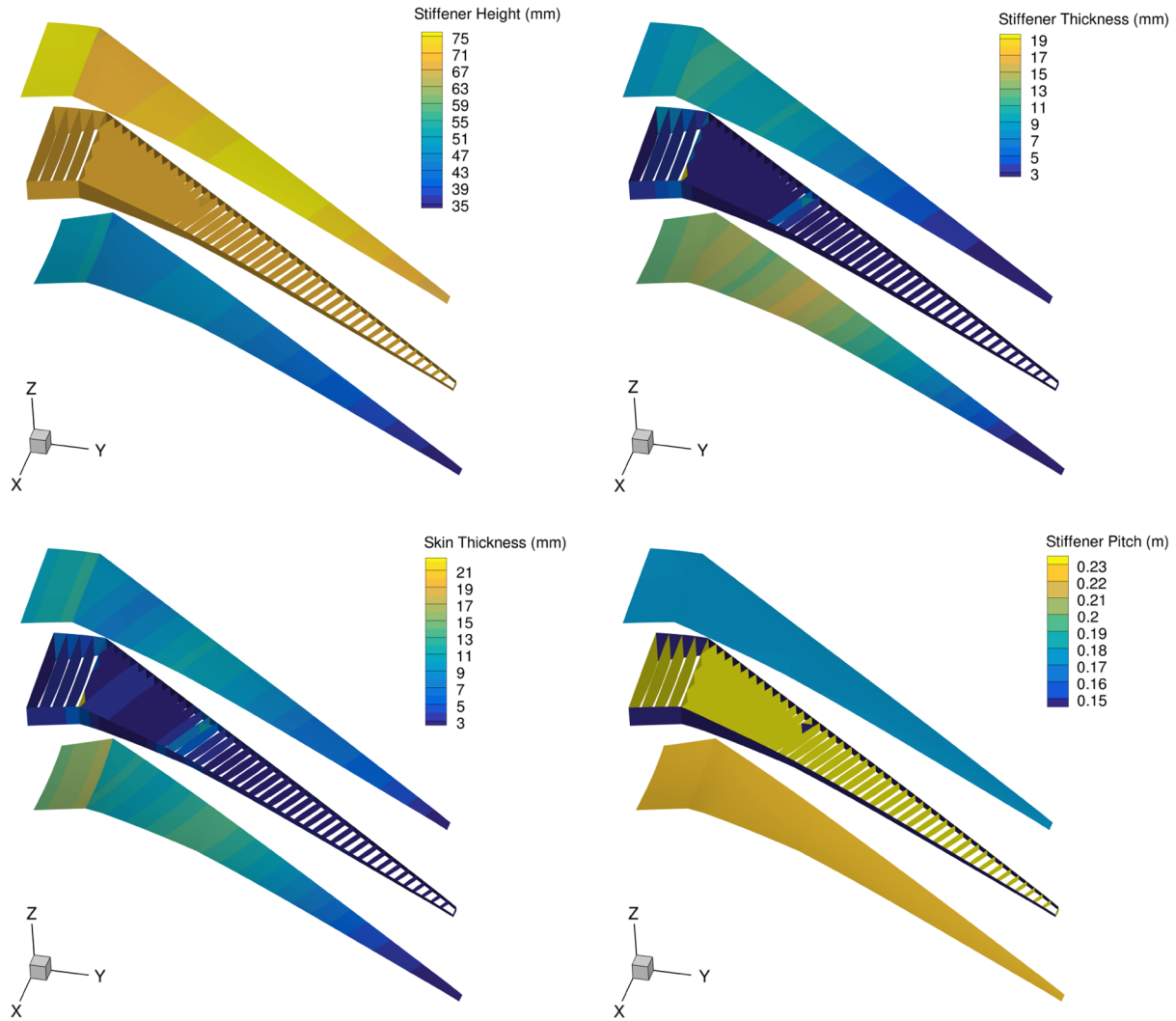


Fig. 6 Distribution of stiffener height, stiffener thickness, skin thickness, and stiffener pitch for the uCRM-9 structural design.

#### Algorithm 1 Inverse-design procedure for uCRM-9

```

1: Set  $X_T \leftarrow \text{surface}\langle 0 \rangle.\text{igs}$ 
2: Set  $n \leftarrow 0$ 
3: Set  $\text{continue} \leftarrow \text{True}$ 
4: while  $\text{continue}$  do
5:    $F = F\langle n \rangle$ 
6:    $\text{FFD} \leftarrow \text{FFD}\langle n \rangle.\text{fmt}$ 
7:    $X_{\text{jig}} \leftarrow \text{surface}\langle n \rangle.\text{igs}$ 
8:   Set  $K \leftarrow \text{wingbox}\langle n \rangle.\text{bdf}$ 
9:   Set  $\text{converged} \leftarrow \text{False}$ 
10:  while not  $\text{converged}$  do
11:     $\text{FFD} \leftarrow x_{\text{dv}}$ 
12:     $X_{\text{jig}} \leftarrow \text{FFD}$ 
13:     $F \leftarrow \text{FFD}$ 
14:     $K \leftarrow X_{\text{jig}}$ 
15:    Solve  $Ku = F$ 
16:     $X_{\text{disp}} \leftarrow u$ 
17:     $I \leftarrow (1/2) \|X_{\text{disp}} - X_T\|$ 
18:    if  $I$  is minimized then
19:       $\text{converged} \leftarrow \text{True}$ 
20:     $F\langle n+1 \rangle = F$ 
21:     $\text{FFD}\langle n+1 \rangle.\text{fmt} \leftarrow \text{FFD}$ 
22:     $\text{surface}\langle n+1 \rangle.\text{igs} \leftarrow X_{\text{jig}}$ 
23:     $\text{wingbox}\langle n+1 \rangle.\text{bdf} \leftarrow X_{\text{surface}}\langle n+1 \rangle$ 
24:    if  $\|X_{\text{surface}}\langle n+1 \rangle - X_{\text{surface}}\langle n \rangle\| < \epsilon$  then
25:       $\text{continue} \leftarrow \text{False}$ 
26:    else
27:       $n \leftarrow n + 1$ 
    ▷ Set CRM wing target coordinates
    ▷ Set iteration counter
    ▷ Set inverse design procedure convergence flag
    ▷ Begin inverse design procedure
    ▷ Read the forces on the current surface mesh
    ▷ Read the current FFD file
    ▷ Read the current surface file
    ▷ Assemble FEM stiffness matrix using current structural mesh
    ▷ Set optimization convergence flag
    ▷ Start optimization loop; minimize  $I$  with respect to FFD variables
    ▷ Update FFD with new optimization design variables
    ▷ Update jig shape with current FFD design variables
    ▷ Update force locations with current FFD design variables
    ▷ Update FEM stiffness matrix
    ▷ Evaluate structural displacements
    ▷ Extrapolate displacement to wing surface to find displaced shape
    ▷ Evaluate objective
    ▷ Check optimization convergence (Karush–Kuhn–Tucker conditions)
    ▷ Update the positions of the tractions on approximate jig shape
    ▷ Generate new FFD file using the current design variables.
    ▷ Generate new surface file,  $\text{surface}\langle n+1 \rangle.\text{igs}$ 
    ▷ Generate new structural wingbox based on  $\text{surface}\langle n+1 \rangle$ 
    ▷ Check if continuous surface has changed
    ▷ If not, end design procedure
    ▷ If so, increment iteration counter

```



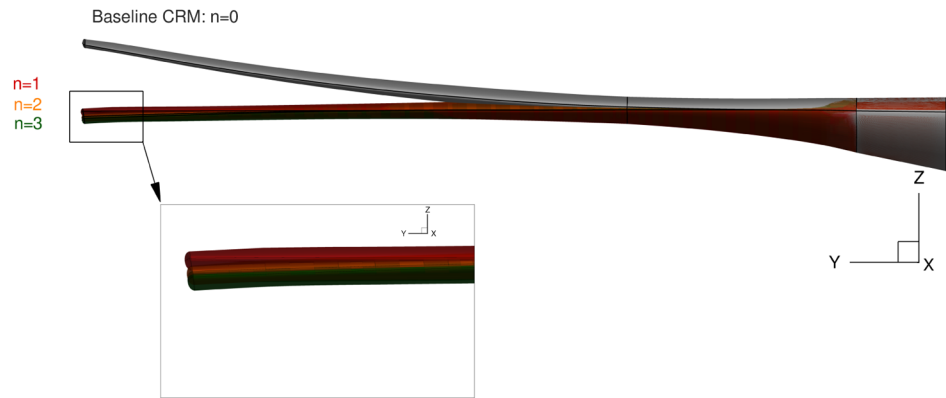


Fig. 7 Inverse design iteration history for uCRM-9 wing jig.

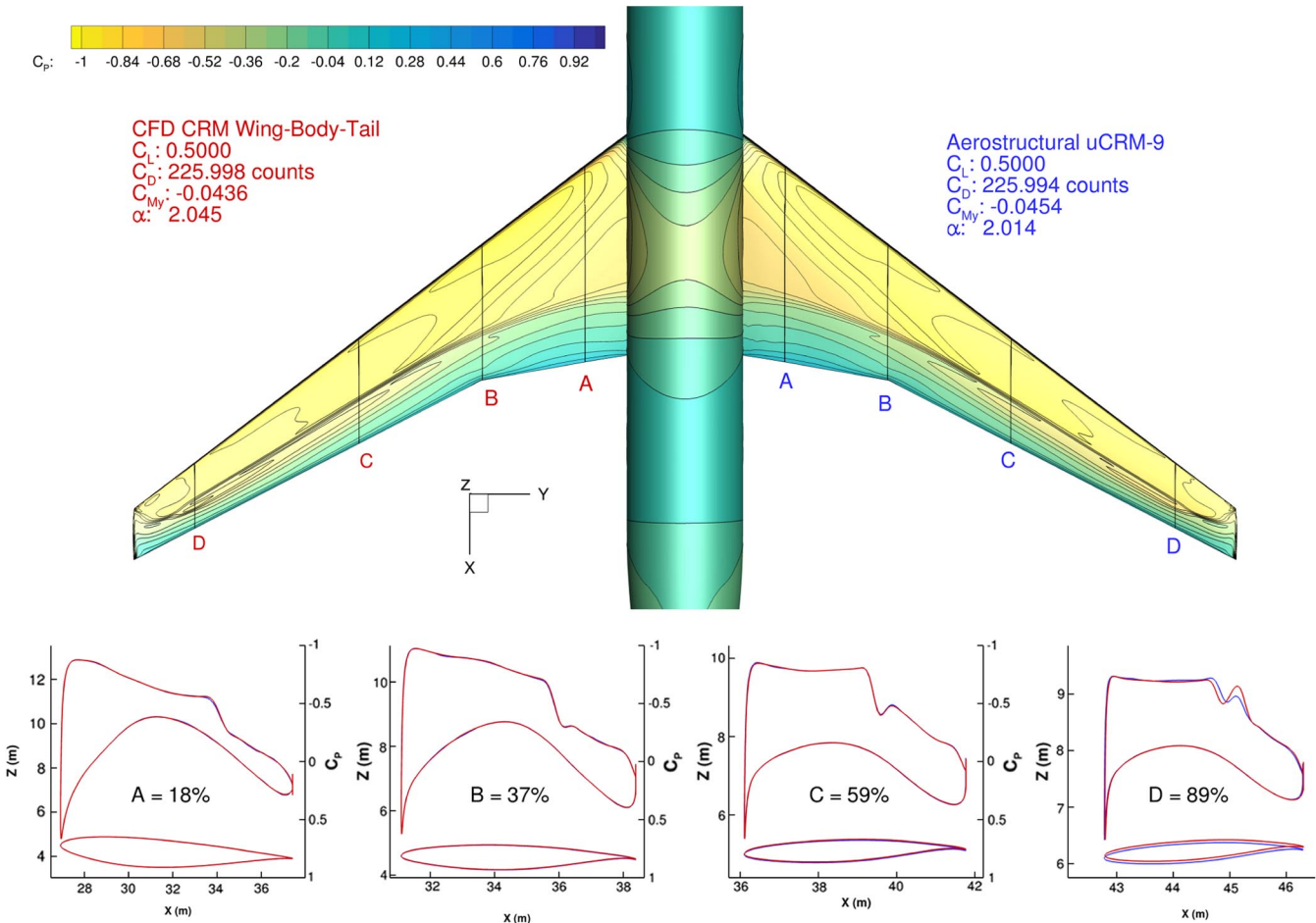


Fig. 8  $C_p$  contour comparison of original CRM geometry CFD solution and uCRM aerostructural solution.

analysis of the model about its nominal cruise condition with three levels of CFD-FEM mesh refinement: coarse, medium, and fine. The fine meshes are the same CFD-FEM meshes used in the aerostructural verification described in Sec. III.D. To obtain the coarse meshes, we coarsen the fine CFD mesh by a factor of 8 and coarsen the fine FEM mesh by a factor of 4. The medium meshes are obtained by creating a mesh size family between the fine and coarse grids. The sizes of CFD-FEM meshes used in this study are listed in Table 3.

Table 3 uCRM-9 CFD and FEM grid sizes			
Quantity	Coarse	Medium	Fine
CFD cells	1,232,948	3,629,280	9,822,874
FEM DOFs	142,428	356,328	571,716

Next, we perform an aerostructural analysis on the uCRM-9 model, matching  $C_L$  for all three grid levels. Figure 9 compares the aerodynamic and structural solutions and shows the mesh size for all three grid levels. The aerodynamic results show that the pressure distribution on the wing looks similar overall, differing only slightly near the shock as the mesh is refined. Similarly, on the structural model, we see that the von Mises stress distribution is relatively insensitive to mesh size, confirming that the structural model has an adequate number of DOFs.

Table 4 lists additional aerodynamic and structural metrics of interest for this refinement study. Although we see that all three mesh levels produce similar results, we can highlight several trends. First, we notice that, as the mesh is refined,  $C_D$  decreases. This is no surprise because, as the CFD mesh is refined, the spurious drag caused by the numerical viscosity of the model decreases. In addition

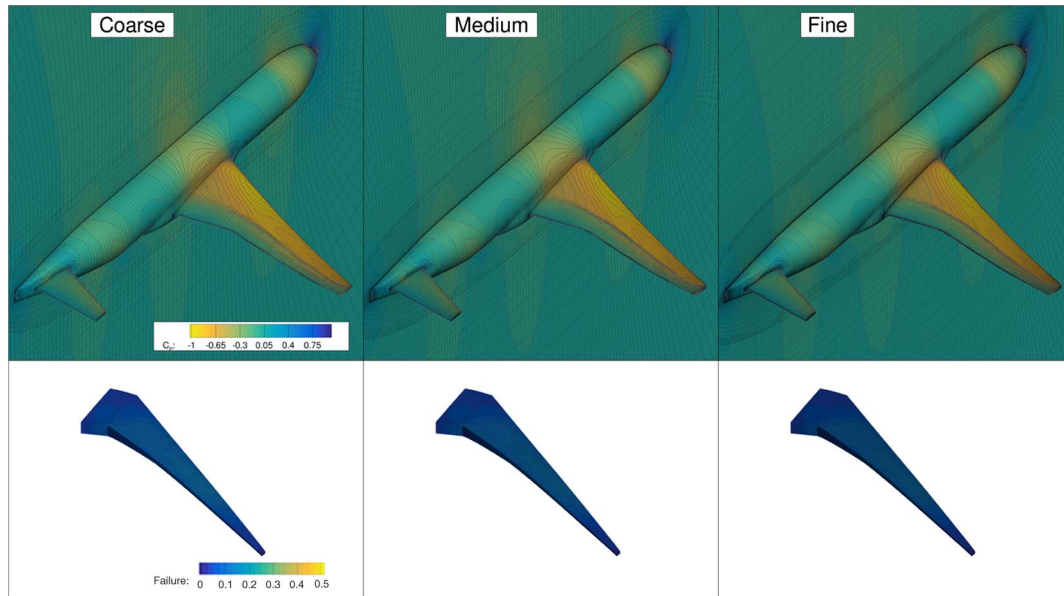


Fig. 9 Aerostructural solutions for uCRM-9 grid convergence study. Aerodynamic pressure coefficient contours (top) and von Mises structural stress values as a fraction of yield stress (bottom).

to this, we see that the displacement of the wing tip increases slightly as the mesh is refined. This is a general trend expected in FEM theory, where the stiffness of a structure decreases with the number of DOFs. In Fig. 10, we plot the drag as a function of grid factor for each grid. This plot shows that all three grid solutions lie along the Richardson extrapolation line, showing that we are in the asymptotic convergence region expected for a second-order CFD scheme.

#### IV. uCRM-13.5 Definition

The uCRM-13.5 model is the result of a full aerostructural design optimization where the wing OML and the structural sizing are optimized simultaneously. This is in contrast with the uCRM-9 model, where the CRM OML is preserved, and only the structural sizing is optimized. The uCRM-13.5 wing remains compatible overall with the remainder of the CRM aircraft but is meant to represent the higher-AR wings that are expected in future aircraft. In this way, the resulting aircraft is a higher-span derivative of the CRM. The goal of this model is to develop a straightforward modification of the well-tested CRM configuration with a clear connection to that configuration. The extension of uCRM-9 to obtain the required 13.5 AR is complicated by the fact that we want to preserve the same wing loading and landing-gear location to avoid a cascade of design changes that would affect the preliminary sizing. Keeping in mind the constraints imposed by a common fuselage, empennage, and propulsion system, we decided to keep the reference area fixed.

##### A. Planform and General Characteristics

The uCRM-13.5 wing planform is designed by first taking the uCRM-9 planform and extending the wing span until reaching an AR of 13.5, as specified by NASA [40]. As was done for the uCRM-9, the uCRM-13.5 reference area is based on the Wimpres area (see Fig. 11). The wing Wimpres area is kept constant to ensure that the wing loading remained unchanged. Although the Wimpres area remains unchanged, the gross wing area (full projected area, including the area covered by the fuselage) increases by 2.2%.

Table 4 uCRM-9 aerostructural grid convergence results

Quantity	Coarse	Medium	Fine
Angle of attack, deg	2.044	2.026	2.019
$C_D$ , counts	238.9	229.9	226.0
$C_{M_y}$	-0.0441	-0.0445	-0.0454
Tip displacement, m	2.591	2.592	2.594

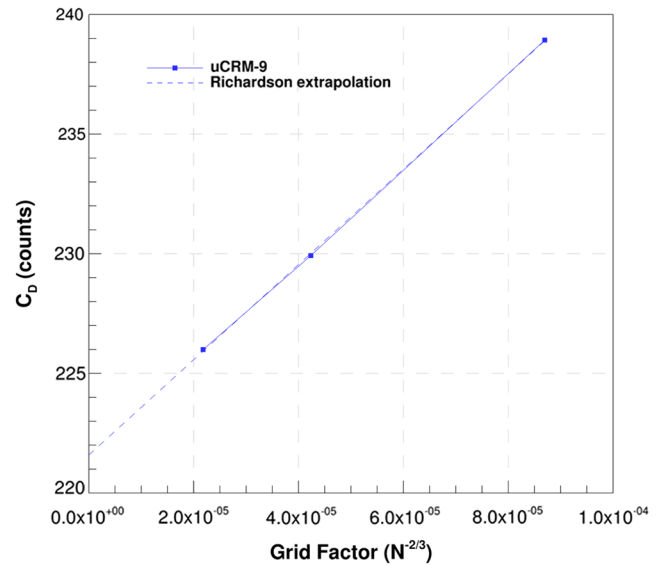


Fig. 10 Aerostructural drag convergence for uCRM-9.

The uCRM-13.5 has a smaller taper ratio of 0.25 compared with the taper ratio of 0.275 for the uCRM-9. In addition to this, the Yehudi break spanwise location moves from 37 to 40% span. These changes are made to maintain a constant Wimpres area while ensuring adequate space for the landing gear. Figure 12 compares the uCRM-13.5 planform with that for the uCRM-9.

To minimize changes in the aircraft longitudinal stability, the entire uCRM-13.5 planform is shifted forward to align the quarter-chord MAC location with the uCRM-9 reference-point location (also at the quarter-chord MAC location). This leaves the nominal moment arm of the horizontal and vertical stabilizers unchanged and offers the additional benefit of distributing the movement in the side of the body chord to the leading and trailing edges, thereby minimizing any changes required to the wing-body fairing. Figure 13 shows three views of the uCRM-13.5 planform. Note that, like the uCRM-9, the uCRM-13.5 has no built-in dihedral. The key geometric parameters of the uCRM-9 and uCRM-13.5 planforms are listed in Table 5.

Figure 13 also shows the structural wingbox planform. We design the uCRM-13.5 wingbox to have the same topology as the uCRM-9, with the exception of the number of ribs. To preserve the buckling loads of the skin panels, the absolute rib spacing is kept the same, and



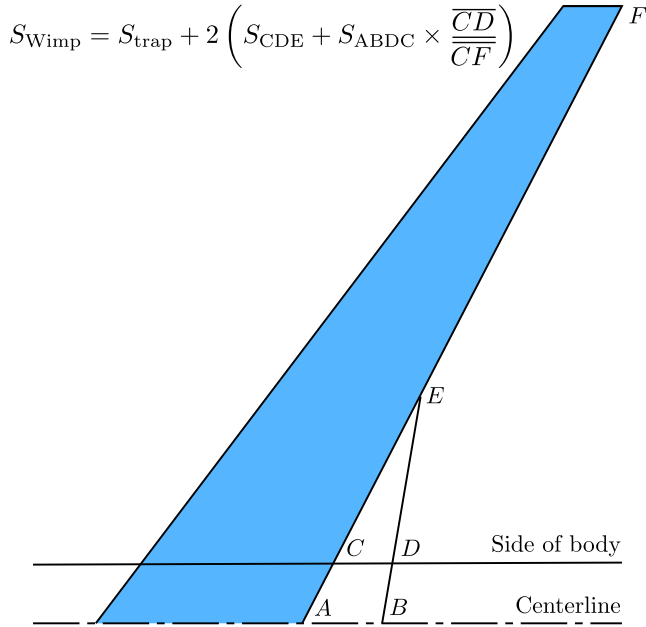


Fig. 11 Wimpres wing reference area definition.

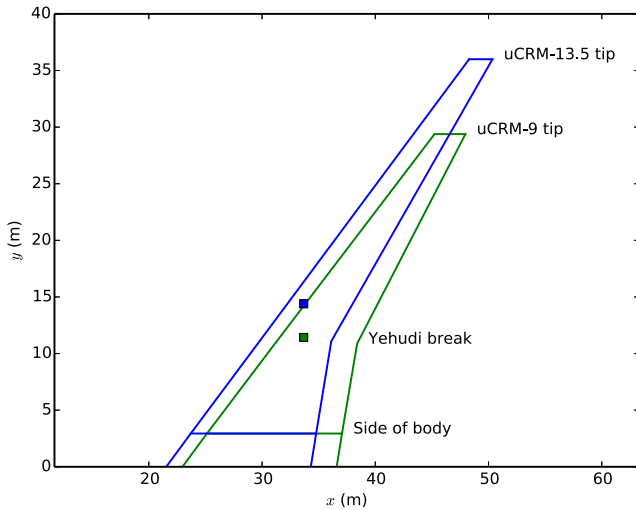


Fig. 12 Comparison of the uCRM-13.5 (blue) and uCRM-9 (green) wing planforms with locations of 1/4 chord MAC (squares).

so the uCRM-13.5 has nine additional ribs for a total of 58. The trailing-edge spar also features a more distinctive kink at the Yehudi break. This is done to move the spar forward in this region and to ensure that the spar depth does not become so small as to become a manufacturing concern. The engine is also assumed to be mounted in the same absolute spanwise position.

### B. uCRM-13.5 Aerostructural Design Optimization

Similarly to the uCRM-9, we base the uCRM-13.5 on a traditional aluminum wingbox structure. A 13.5 AR wing is pushing the limits of what is currently possible with conventional aluminum wing design. As a result, an aerostructural analysis of this model, while maintaining a cross-sectional, twist, and structural sizing distribution similar to those of uCRM-9, reveals that this design performs poorly due to the additional structural deformation caused by the increased wing flexibility. For this reason, unlike for the uCRM-9, we optimize the full aerostructural design to take these effects into account and obtain an optimal wing for the uCRM-13.5 configuration. Buffet-onset constraints are also enforced in the design optimization to obtain a wing that can be used for a transonic transport aircraft that meets U.S. Federal Aviation Administration (FAA) regulations.

In the remainder of this section, we provide a complete description of the design optimization problem that we use to obtain the uCRM-13.5 benchmark model. The initial wing mass is estimated from a structural optimization performed before the aerostructural optimization. The CFD and FEM meshes used for the optimization are based on the coarse grids introduced in Sec. III but adapted for the uCRM-13.5 wing planform. The structural model used in this optimization features second-order shell elements with a mixed interpolation of tensorial components [30,41], and with a total of 190,710 DOFs. A wing-body-tail overset CFD mesh consisting of a total of 1.23 million volume cells is used to compute the aerodynamics.

The flight conditions considered consist of a five-point cruise stencil, two buffet constraint conditions, and three maneuver conditions. The initial optimization flight conditions are listed in Table 6, where MTOW is the maximum takeoff weight of the aircraft. The five cruise design conditions form a cross in Mach- $C_L$  space, which is done to ensure that the fuel burn of the design is robust with respect to aircraft weight and flight speed. The center of the cruise stencil, condition 1, corresponds to the nominal CRM cruise condition ( $M = 0.85$ ,  $C_L = 0.5$ ). Conditions 2 and 3 are offsets of  $\pm 0.025$  in  $C_L$  relative to the nominal cruise condition. Conditions 4 and 5 are offsets of  $\pm 0.01$  in Mach number relative to the nominal condition, with the constraint that they maintain the same physical lift.

The two buffet conditions are chosen to constrain buffet onset at two points: a high-lift condition, and a high-Mach-number condition. The first buffet point applies a 1.3g margin on the highest lift at cruise (condition 3). The second buffet condition is at  $M = 0.89$ , with the constraint that the lift match that of the nominal cruise (condition 1). All buffet and cruise conditions are evaluated at an altitude of 37,000 ft. Similar to the uCRM-9, the uCRM-13.5 is structurally sized not to exceed the yield stress or buckling load at the  $-1g$  and  $2.5g$  maneuver conditions. In addition, a  $1g$  cruise gust condition is added to the structural sizing analysis. The purpose of the cruise with gust flight condition is to provide a case that structurally sizes the wing for conditions when the aircraft experiences a sudden gust load around cruise but is not allowed sufficient time to shift the loads inboard through passive load alleviation. We model the loads for the gust condition by analyzing the static cruise loads of the design at the Mach crossover point and applying a 1.3 load factor to the aerodynamic loads [42].

#### 1. Objective

The objective of the optimization is to minimize the average fuel burn at the cruise conditions. For this optimization, the fuel burned during the taxiing, takeoff, climb, and descent phases of the flight is neglected. The fuel burn for each cruise condition is computed by using the Breguet range equation:

$$FB_i = LGW \left[ \exp \left( \frac{Rc}{V_{\infty_i} (L/D)_i} \right) - 1 \right] \quad (1)$$

where LGW is the aircraft landing weight,  $R$  is the range,  $c$  is the thrust-specific fuel consumption of the engine, and  $V_{\infty_i}$  and  $(L/D)_i$  are the flight speed and lift-to-drag ratio at cruise condition  $i$ , respectively. To compute the objective, we take a weighted average of the fuel burns from all five cruise conditions:

$$Obj = \sum_{i=1}^N T_i \times FB_i \quad (2)$$

In this case, the weightings of each condition are set to be equal,  $T_i = 1/5 \forall i$ .

Because the model does not include the vertical tail or engine nacelles and corresponding pylons, 35 counts of drag are added to the CFD-computed drag coefficient to account for these missing components. The landing weight of the aircraft is computed from the wingbox FEM along with a set of fixed weight components (fuselage, payload, nonstructural masses, and engines) by using the following formula:

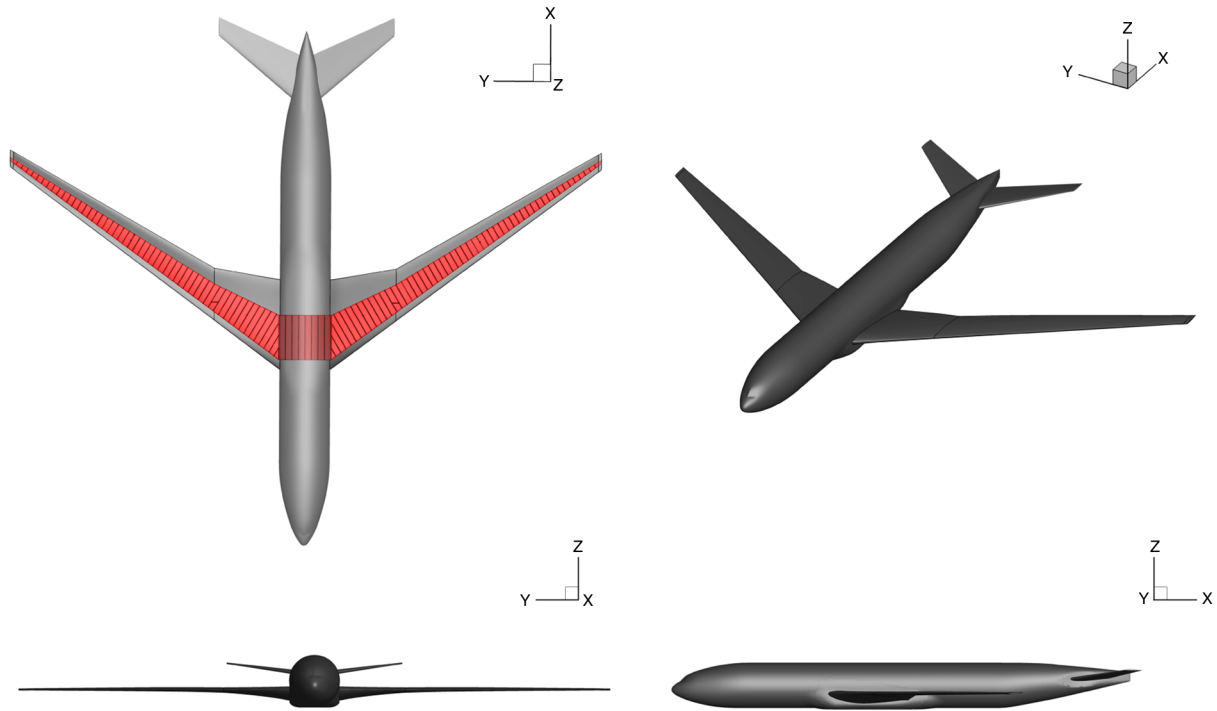


Fig. 13 Three-view of uCRM-13.5 wing planform and structural geometry.

$$\text{LGW} = 1.25 \times W_{\text{box}} + \text{Fixed Weight} + \text{Reserve Fuel Weight} + \text{Secondary Wing Weight} \quad (3)$$

where  $W_{\text{box}}$  is the weight computed by the wingbox structural model. The factor of 1.25 accounts for additional weight associated with fasteners, overlaps, and other components not modeled in the idealized wingbox. Table 7 lists the remaining design parameters used to compute the objective function.

## 2. Design Variables

To take full advantage of the possible gains in high-fidelity aerostructural wing design optimization, a large number of design variables is required. In RANS-based aerodynamic shape optimization, Lyu et al. [5] showed that at least 200 wing shape variables are required to achieve a good tradeoff between the optimal result and the number of variables. For structural sizing based on detailed wingbox FEMs, the more sizing variables that are included, the more the optimizer can reduce the weight and leave material only where it is actually needed. The design variables can be broken down into three groups: geometric variables, aerodynamic variables, and structural variables. A total of 1112 design variables are used for this design optimization (see list in Table 8).

The geometric design variables include the airfoil cross-sectional shape distribution over the span of the wing. The optimizer controls

these shapes by perturbing the  $z$  coordinate of each control point on the FFD surface containing the wing, shown as red spheres in Fig. 1. The optimizer also controls the spanwise twist distribution of the wing by rigidly rotating each chordwise set of FFD control points. The optimizer cannot change the planform (sweep, span, and reference area) because we want to keep it fixed for the design.

The aerodynamic design variables include the angle of attack for each of the 10 flight conditions. The angle-of-attack variables are necessary to satisfy the lift constraint for each condition. In addition to the angle-of-attack variables, we also include a horizontal stabilizer incidence angle variable for each flight condition. This

Table 6 Initial uCRM-13.5 flight condition stencil

Number	Condition	Mach number $M$	$C_L$ /Lift	Altitude, ft
1	Cruise	0.85	0.500	37,000
2	Cruise	0.85	0.475	37,000
3	Cruise	0.85	0.525	37,000
4	Cruise	0.84	0.512	37,000
5	Cruise	0.86	0.488	37,000
6	Buffet	0.85	0.683	37,000
7	Buffet	0.89	0.456	37,000
8	2.5g maneuver	0.64	$2.5 \times \text{MTOW}$	0
9	-1g maneuver	0.64	$-\text{MTOW}$	0
10	Cruise with gust	0.86	MTOW	27,300

Table 5 uCRM specifications

Parameter	uCRM-9	uCRM-13.5
Aspect ratio	9.0	13.5
Span, m	58.76	72.00
Side of body chord, m	11.92	11.07
Yehudi chord, m	7.26	6.34
MAC, m	7.01	5.77
Tip chord, m	2.736	2.06
Wimpres reference area, m <sup>2</sup>	383.74	383.78
Gross area, m <sup>2</sup>	412.10	421.08
Exposed area, m <sup>2</sup>	337.05	351.02
1/4 chord sweep, deg	35	35
Taper ratio	0.275	0.250
Gear post depth, m	0.736	0.648

Table 7 Design optimization specifications

Parameter	Value
Initial cruise altitude	37,000 ft
Initial MTOW	297,500 kg
Initial maximum landing weight	213,180 kg
Initial maximum zero fuel weight	195,040 kg
Initial operational empty weight	138,100 kg
Design range	7725 n mile
Design payload	34,000 kg
Reserve fuel	15,000 kg
Initial wing weight	30,286 kg
Fixed weight	107,814 kg
Thrust specific fuel consumption $c$	0.53 lb/(lbf · h)

**Table 8 uCRM-13.5 optimization design variables**

Variable	Description	Quantity
$x_{\alpha_i}$	Angle of attack for each case	10
$x_{\text{tail}}$	Tail trim angle for each case	10
$x_{\text{twist}}$	Wing twist	8
$x_{\text{shape}}$	FFD control points	240
$x_{\text{panel thick}}$	Panel thickness skin, spars, ribs	287
$x_{\text{stiff thick}}$	Panel stiffener thickness skin, spars, ribs	184
$x_{\text{stiff height}}$	Panel stiffener height skin, spars, ribs	184
$x_{\text{panel length}}$	Panel length skin, spars, ribs	184
$x_{\text{stiff pitch}}$	Panel stiffener pitch skin, spars, ribs	4
$C_{L_0}^*$	Nominal cruise target lift coefficient	1
	Total design variables	1112

variable ensures that we can trim out the pitching moment about the aircraft center of gravity for each flight condition.

A target nominal lift coefficient design variable is used to allow the nominal cruise condition to change and ensure an optimal cruise  $C_L$  as the design changes. The other four flight conditions follow this changing nominal condition by using the specified  $C_L$ . Only the cruise and buffet points are affected by the moving stencil because the maneuver conditions are constrained to match the aircraft MTOW. The purpose of allowing the optimizer to move the position of the cruise stencil in  $C_L$  is to provide a means to control the design cruise altitude. This means that, as the nominal cruise  $C_L$  increases, the aircraft has to fly at a higher cruise altitude to carry the same weight.

The remaining design variables consist of the structural design variables used to parameterize the wingbox. These variables include the stiffener pitch of the upper skin, lower skin, leading-edge spar, and trailing-edge spar because the pitch is assumed to be constant across each of these components. As a result of the panel-based smeared-stiffness approach described in Sec. III, three additional design variables are used for each wingbox rib bay section: panel thickness, stiffener thickness, and stiffener height. The only exception to this are the ribs, all of which share stiffener design variables. Additionally, the panel length is included as a design variable for each panel to simplify the panel buckling computations. Because the panel dimensions change with the geometry during optimization, a nonlinear consistency constraint is added for each panel length variable to ensure that they match the respective geometric panel lengths of each component.

### 3. Constraints

To obtain a meaningful and physically realizable design, many constraints must be considered in the optimization problem. Our design optimization enforces a total of 1328 linear and nonlinear constraints, as listed in Table 9.

The first set of these constraints is to ensure steady trimmed flight for each design condition. For the cruise and buffet conditions, this means that the lift coefficient  $C_{L_i}$  for that condition must match the value defined by the moving cruise flight conditions stencil. For the maneuver conditions, the constraint is specified for the physical lift such that the lift equals the MTOW multiplied by the respective load factor  $n$ , where the MTOW is based on the fuel burn computed from the first cruise condition, i.e.,

$$\text{MTOW} = \text{LGW} + \text{FB}_0 \quad (4)$$

We use a separation-based buffet constraint for the two buffet design points. By constraining buffet at these two points, we ensure that all cruise points remain in the envelope defined by the 1.3g margin to buffet onset, as required by flight regulations [24].

The next set of constraints related to the geometry is imposed to prevent physically unrealizable designs. A constraint is imposed on the wing leading-edge radius, preventing it from decreasing relative to the baseline. This is done to prevent the optimizer from compromising the high-lift performance for takeoff and landing, a condition that is not included explicitly in the formulation of the optimization problem. Lyu et al. [5] showed that transonic wing optimizations without this constraint yield designs with unrealistically sharp leading edges.

Additionally, a constraint is applied to the wing trailing edge to prevent the thickness from decreasing. This is done to prevent the optimizer from producing designs with excessively thin trailing edges, which leads to manufacturing and handling problems. Along a similar vein, a constraint is placed on the depth of the wing at the location of the trailing-edge spar. Again, this is done to prevent manufacturing difficulties and to ensure that there is adequate room for the actuators and control surfaces to be mounted on the spar.

A volume constraint is imposed on the fuel bay of the wing to ensure that the volume is sufficient to contain the fuel required to complete the mission, including reserve fuel. The last of the sets of geometric constraints consists of 16 linear constraints on the FFD shape variables that prevent the leading edge from moving vertically relative to the trailing edge. This ensures that no inadvertent twist is added to the wing through the shape variables and guarantees that the twist and shape variables are independent.

The remaining constraints are applied to the structure of the wing. The 2.5g maneuver and 1g cruise with gust conditions each use four KS material failure constraint aggregation functions: one each for the upper and lower skins, and one for the ribs and spars. For these conditions, aggregated buckling constraints are enforced only for the upper skin, ribs, and spars. For the  $-1g$  condition, only the buckling constraints are enforced for the lower skin, ribs, and spars. This is because the  $-1g$  case is not critical in sizing for stress as are the 2.5g and the 1g cruise conditions. As mentioned previously, consistency

**Table 9 Constraints for uCRM-13.5 optimization design**

Variable or function	Description	Quantity
$C_{L_i} = C_{L_i}^*$	Cruise and buffet lift conditions	7
$L = n_i \text{MTOW}$	Maneuver lift conditions	3
$C_{M_y}^* = 0$	Trimmed flight	10
$\text{Sep}_i \leq 0.04$	Buffet separation constraints	2
$t_{LE}/t_{LE,init} \geq 1.0$	Leading-edge radius	20
$t_{TE}/t_{TE,init} \geq 1.0$	Trailing-edge thickness	20
$(t/c)_{TE,spar} \geq 0.80(t/c)_{TE,spar,init}$	Minimum trailing-edge spar height	20
$V - V_{fuel} \geq 0.0$	Minimum fuel volume	1
$L_{\text{panel}} - x_{\text{panel length}} = 0$	Target panel length	266
$\text{KS}_{\text{fail}} < 1.0$	2.5g and gust material failure	8
$\text{KS}_{\text{buckling}} < 1.0$	2.5g, $-1g$ , and gust buckling	9
$ x_{\text{panel thick}_i} - x_{\text{panel thick}_{i+1}}  \leq 0.0025$	Skin thickness adjacency	258
$ x_{\text{stiff thick}_i} - x_{\text{stiff thick}_{i+1}}  \leq 0.0025$	Stiffener thickness adjacency	258
$ x_{\text{stiff height}_i} - x_{\text{stiff height}_{i+1}} $	Stiffener height adjacency	258
$x_{\text{stiff thick}} - x_{\text{panel thick}} < 0.005$	Maximum stiffener-skin difference	172
$\Delta z_{TE,upper} = -\Delta z_{TE,lower}$	Fixed trailing edge	8
$\Delta z_{LE,upper} = -\Delta z_{LE,lower}$	Fixed leading edge	8
	Total constraints	1328



constraints also exist for each panel to ensure that the panel length used for the buckling calculations are consistent with the physical dimensions of the panel. Finally, we apply hundreds of linear adjacency constraints to ensure that the panel thickness as well as the stiffener thickness and heights do not change too abruptly from panel to panel.

### C. Results

In addition to the uCRM-13.5 design produced by the optimization procedure described in the previous section, we also provide the baseline nonoptimized uCRM-13.5 design as a reference. This design features the initial uCRM-13.5 planform extended from the uCRM-9, where the cross-sectional shapes, twist distribution, and

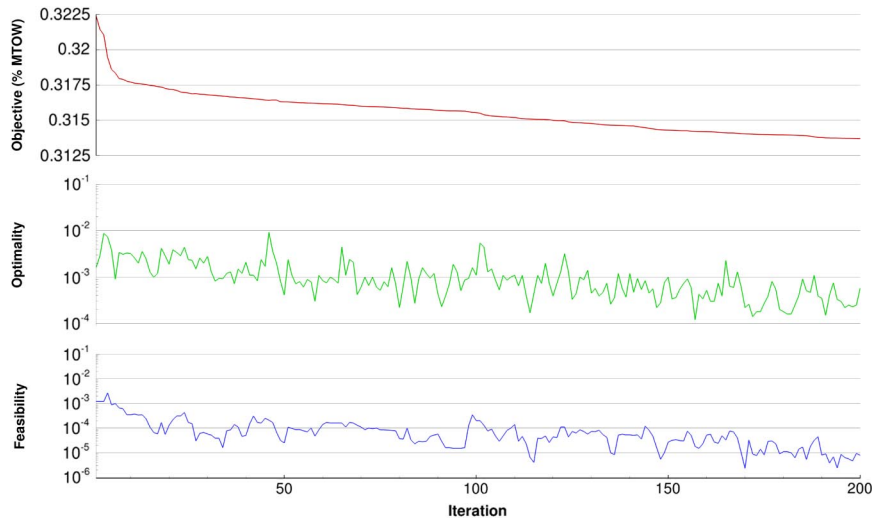


Fig. 14 Convergence history for the uCRM-13.5 aerostructural optimization.

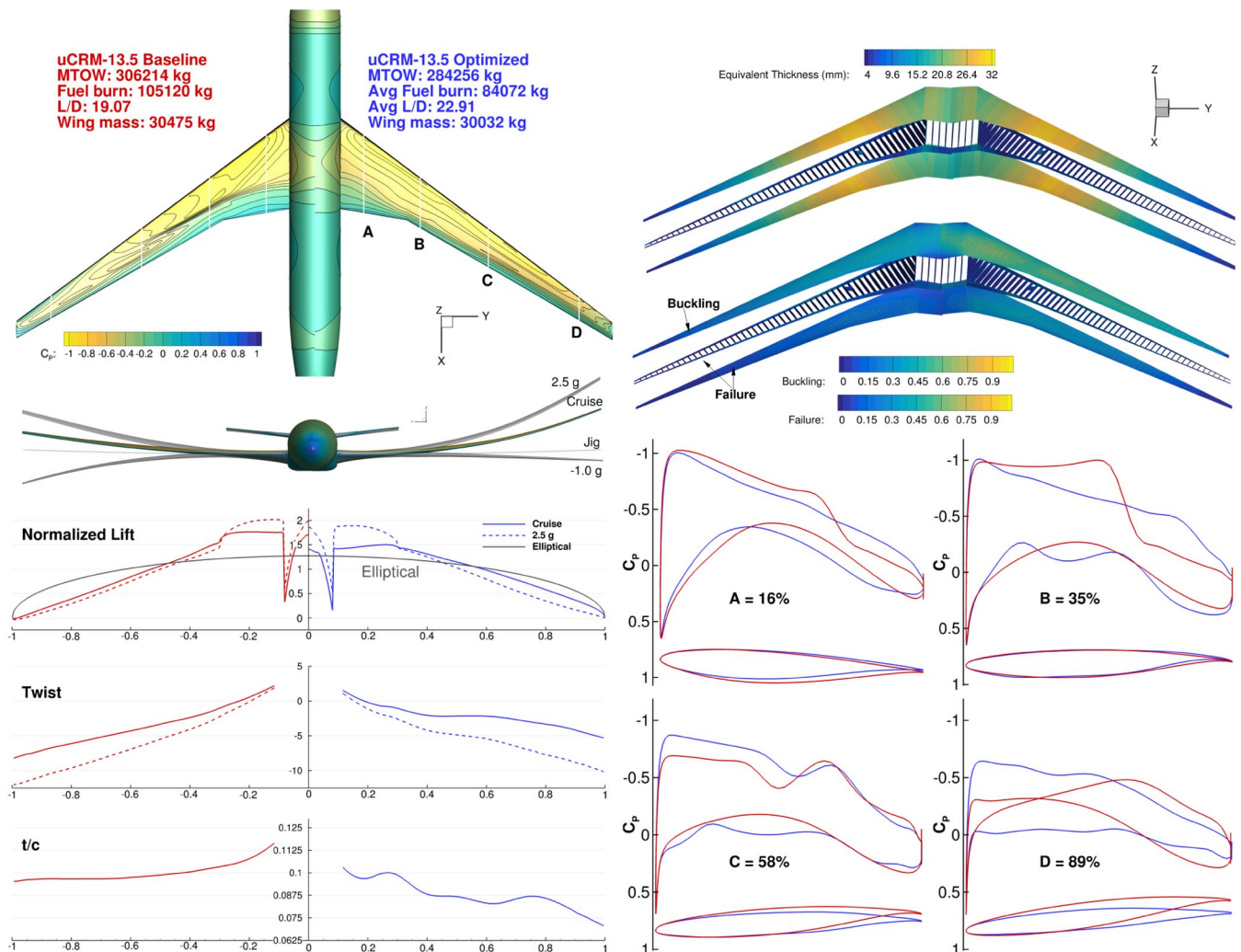


Fig. 15 Aerostructural design of the uCRM-13.5 baseline (left) compared with that of the optimized uCRM-13.5 (right).

**Table 10** Optimized uCRM-13.5 final flight condition stencil

Point	Condition	Mach	$C_L$
1	Cruise	0.85	0.549
2	Cruise	0.85	0.524
3	Cruise	0.85	0.574
4	Cruise	0.84	0.562
5	Cruise	0.86	0.536
6	Buffet	0.85	0.746
7	Buffet	0.89	0.501

structural-sizing distribution are all fixed. As mentioned previously, because the aeroelastic properties differ greatly between the uCRM-9 and the uCRM-13.5 due to the increase in wing flexibility, we can expect this design to perform poorly. Therefore, we reoptimized it.

The optimization was run on 1000 processors (roughly 100 processors per flight condition) and took about 48 h. Figure 14 shows the iteration history for the optimization. The objective function is the fuel burn as a fraction of the design MTOW. The feasibility and optimality are a measurement of the constraint violation and satisfaction of the first-order Karush–Kuhn–Tucker conditions, respectively [33]. The optimizer gradually reduces the objective while improving the feasibility of the design. The optimization is terminated after 200 major iterations. The objective function decrease flattens out in the last 10 iterations, at which point subsequent improvements are less than 1.5 kg (about 0.002%).

Figure 15 compares the resulting optimized uCRM-13.5 design with the nonoptimized baseline. The top-left corner of the figure shows the cruise  $C_p$  distribution of each design and a front view with the deflection of the wing at various flight conditions. Below that, we show spanwise aerodynamic quantities of interest: normalized lift distribution, wing twist, and wing thickness-to-chord ratio  $t/c$ . The upper-right corner shows the structural values of interest: the mass equivalent structural thickness distribution of the wingbox panels and the buckling and material failure constraints for the 2.5g maneuver condition (the most restrictive of the maneuver conditions) over each wingbox component. Finally, below this, we show four airfoil slices and the corresponding  $C_p$  distributions at various spanwise locations along the wing. Additionally, the optimized design is free to translate its cruise and buffet design conditions with respect to  $C_L$  during the optimization. The final flight conditions for the optimized design are listed in Table 10.

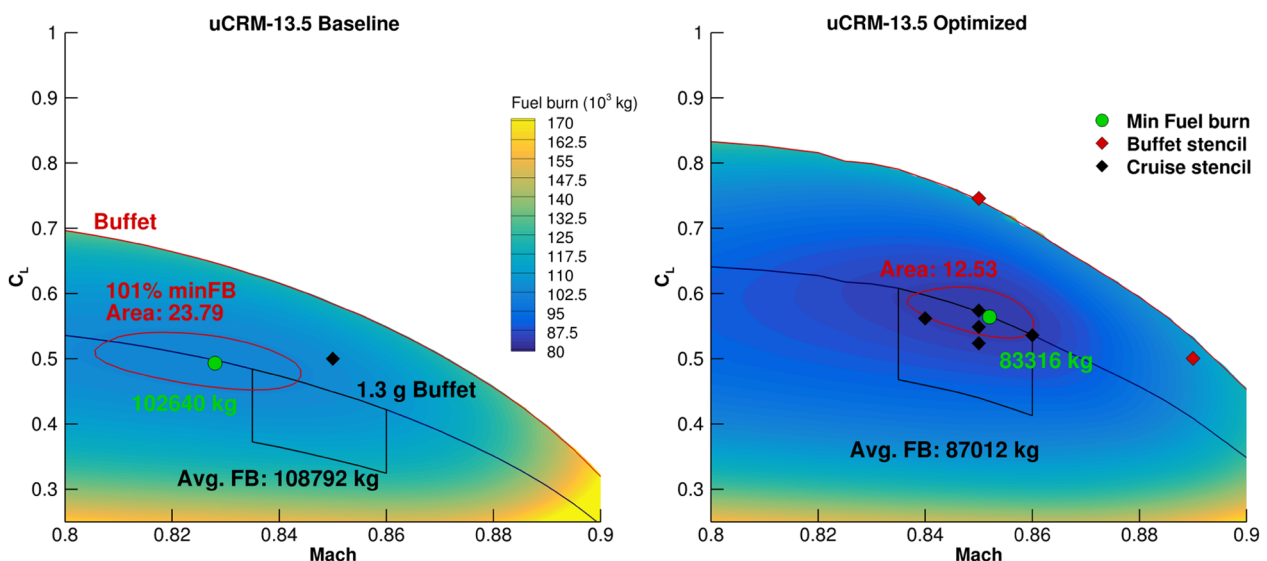
Figure 15 shows several key differences between the baseline and optimized uCRM-13.5 designs. First, the optimized aircraft benefits from a 20% improvement in fuel burn performance (21,048 kg). Comparing the  $L/D$  ratios for both designs reveals that the difference

in fuel burn is primarily due to the poorer aerodynamic performance of the baseline design. In addition, comparing the normalized lift and twist distributions yields further insight into how the optimizer improves the aerodynamic performance. The optimization gives a more elliptically loaded spanwise lift distribution at cruise, which reduces the induced drag on the wing. The nonelliptical lift distribution of the baseline design is due to the wing featuring too much washout at the tips, which means that very little lift is generated in the outboard region of the wing, so that the inboard lift has to increase to compensate. In addition to causing the lift distribution to deviate from elliptical, which increases the induced drag, this also causes a strong shock to occur in the inboard region of the wing, increasing the wave drag. The optimizer removes the additional washout by twisting the wing tips up, leading to a more aerodynamically efficient design. The distribution of  $t/c$  shows that the optimizer reduces the airfoil thickness of the wing to decrease the drag. A lower  $t/c$  ratio also mitigates flow separation, improving the buffet onset constraint, which allows the optimized design to fly at a slightly greater  $C_L$ , thereby improving the ratio  $L/D$ .

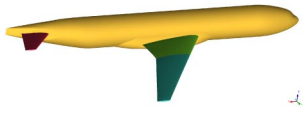

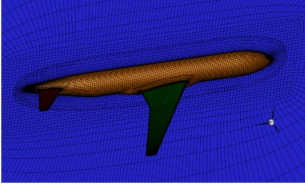
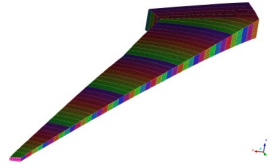
Figure 16 shows a fuel-burn contour plot as a function of Mach and  $C_L$  for both designs. This plot corresponds to different flight performances for the design at varying flight speeds and aircraft weights. By using this plot, we can evaluate both the robustness of each design and the margin between buffet onset and the cruise flight envelope. The line denoted “1.3g buffet” in the left panel of Fig. 16 indicates the boundary for all operational conditions that have at least a 1.3g margin to buffet onset. Ideally, to comply with FAA regulations, all points in the cruise stencil would lie below this line. We see that, for the nominal cruise condition, the baseline uCRM-13.5 design is not within this feasible region, which emphasizes the importance of considering buffet onset in the design optimization for the uCRM-13.5.

The box under the 1.3g buffet boundary line in Fig. 16 is called the fuel-burn performance integration region. We average the fuel burn in this region to assess the real-world performance of the design. Ideally, this region should overlap with the cruise stencil, and both should lie close to the global minimum fuel burn on the plot. However, because the buffet boundary is so restrictive in the case of the baseline uCRM-13.5 design, the integration region, nominal cruise point, and minimum fuel burn condition do not align in Mach– $C_L$  design space, thereby reducing the average fuel-burn performance. We see that the optimizer raises the performance integration region by moving the stencil up in  $C_L$  on the optimized uCRM-13.5, which ultimately leads to a decrease of 20.0% in average fuel burn.

To measure robustness, we also plot in red the contour corresponding to 101% of the minimum fuel burn for each design and compute the area enclosed by this contour. This gives us an idea of how quickly the design performance decays from the optimal design

**Fig. 16** Fuel-burn performance contours of each design as well as buffet and 1.3g margin to buffet envelopes.

**Table A1** uCRM file descriptions

File	Description	Image
uCRM-#_wbt.igs/ uCRM-#_wbt.tin	uCRM OML geometry file including the jig wing, fuselage, and horizontal stabilizer. To generate a different CFD mesh, this file can be used as the underlying geometry. We include the files in an IGES format for general use and in a .tin format for use with the meshing software ICEMCFD.	
uCRM-#_wingbox.igs/ uCRM-#_wingbox.tin	Geometry for wingbox structure. Can be used to generate different structural meshes. This file was used with ICEMCFD to produce the NASTRAN bulk-data format (BDF) files listed below. The wingbox is geometrically “perfect” (all surface edges are coincident and do not require any manual cleanup before meshing).	
uCRM-#_wbt_level.cgns	CFD volume meshes for each model. The files come in three different mesh levels: coarse, medium, and fine. The different mesh levels have roughly 1.23, 3.63, and 9.82 million volume cells, respectively. Both structured multiblock and overset meshes are provided.	
uCRM-#_wingbox_level.bdf	Nastran BDF file for the meshed wingbox geometry. The files come in three different mesh levels, corresponding to the three CFD mesh levels: coarse, medium, and fine. The different mesh levels feature roughly 25,000, 61,000, and 98,000 second-order shell elements, respectively. Boundary conditions, material properties, and external masses are also specified.	
uCRM-#_aero_forces_1.0g_level.bdf	Separate loads file for the coarse mesh. This set of loads applied to the uCRM-#_wingbox_coarse.bdf model yields the 1g deflected geometry.	—

point, which translates to robustness with respect to flight conditions. The baseline uCRM-13.5 design has the larger 101% contour region, meaning that it is the more robust design. However, despite its robustness, it is consistently outperformed by the optimized design at any given point in this region of the flight envelope. From this, we conclude that the optimizer is able to improve the fuel burn over the entire flight envelope while keeping the design robust because the optimized design considers performance at multiple flight conditions. For the uCRM-13.5, because the baseline performs so poorly, the logical strategy is to choose the aerostructurally optimized version as the final benchmark model.

## V. Conclusions

This work was motivated by the current lack of benchmark aeroelastic models for transonic aircraft analysis and design. The NASA CRM, which is an excellent and widely used aerodynamic model, was used to develop two static aeroelastic models: one with a conventional AR, and another with a higher AR to be representative of next-generation wings. To accurately capture the appropriate physics associated with transonic flexible wing design, a coupled high-fidelity MDO approach was used to define both aerodynamic and structural models for each configuration. All geometries were based on the jig (undeflected) wing shape, and so the models were appropriate for aerostructural and aeroelastic analysis, as well as for wing aerostructural design optimization studies.

The first model, the uCRM-9, has a wing design with an AR of 9 that deforms into the CRM geometry under its nominal cruise flight condition of  $M = 0.85$ ,  $C_L = 0.5$ . This design was obtained by first defining a wingbox planform and topology for the CRM and sizing it through a structural optimization subject to aerodynamic loads. An inverse design procedure was then executed, where the deflection of the CRM wing was iteratively removed from the geometry by using wing shape variables. The procedure was iterated several times until the result converged. To verify that the design procedure produced an accurate jig shape of the CRM wing, a static aerostructural analysis was performed, and it was found that the drag obtained by the model

was within 0.001% of the drag produced by a CFD analysis of the CRM about its nominal cruise conditions. Finally, the aerostructural grid convergence for the model was studied, which showed that the meshes used to create this model yield good convergence.

The second aeroelastic model, the uCRM-13.5, is a higher-aspect-ratio wing variant of the CRM. The motivation behind this model was to study new technological concepts with the goal of enabling higher-aspect-ratio wing designs for next-generation commercial transport aircraft. Because of the higher flexibility present in the wing design, aerostructural optimization was used to obtain the optimal geometry and structural sizing for this model. This study demonstrated the need to consider multiple flight conditions in the optimization to achieve a robust design. The multipoint optimized design achieved a 20.0% reduction in average fuel burn over its integrated flight envelope relative to the baseline design. In addition, the flight envelope was extended thanks to the inclusion of buffet onset constraints, again demonstrating the necessity for buffet-onset considerations when performing transonic wing design optimization.

All models developed in this work are publicly available and include files for the geometry, structures, and external mass distributions. A detailed description of the publicly available files<sup>††</sup> is included in the Appendix. These models provide a benchmark for future high-fidelity aerodynamic, structural, and aeroelastic studies, both static and dynamic. Further developments are expected to result in variable-fidelity models and models that better capture dynamic aeroelastic phenomena.

## Appendix : Model Files

The files for the uCRM models (both uCRM-9 and uCRM-13.5) are publicly available (see footnote <sup>††</sup>). The included files are listed in Table A1.

<sup>††</sup>Data available online at <http://mdolab.engin.umich.edu/ucrm> [retrieved 7 May 2018].



## Acknowledgments

The authors acknowledge support from NASA through award number NNX11AI19A. The authors also thank Christine Jutte, Bret Stanford, and Karen Taminger of NASA Langley Research Center for their help in defining these models. The authors would like to specifically thank Bret Stanford for providing weights and positions for the external masses used in both models. The authors would lastly like to thank Professor Cesnik from the University of Michigan for his advice during the development of these models. This work used the Extreme Science and Engineering Discovery Environment, which is supported by National Science Foundation grant ACI-1053575.

## References

- [1] Schmitt, V., and Charpin, F., "Pressure Distributions on the ONERA-M6-Wing at Transonic Mach Numbers," Rept. 138, Office National d'Etudes et Recherches Aérospatiales, Chatillon, France, 1979.
- [2] Brodersen, O., and Stuermer, A., "Drag Prediction of Engine-Airframe Interference Effects Using Unstructured Navier-Stokes Calculations," *19th AIAA Applied Aerodynamics Conference*, AIAA Paper 2001-2414, June 2001.  
doi:10.2514/6.2001-2414
- [3] Vassberg, J. C., DeHaan, M. A., Rivers, S. M., and Wahls, R. A., "Development of a Common Research Model for Applied CFD Validation Studies," *26th AIAA Applied Aerodynamics Conference*, AIAA Paper 2008-6919, Aug. 2008.
- [4] Keye, S., Brodersen, O., and Rivers, M. B., "Investigation of Aeroelastic Effects on the NASA Common Research Model," *Journal of Aircraft*, Vol. 51, No. 4, April 2014, pp. 1323-1330.  
doi:10.2514/1.C032598
- [5] Lyu, Z., Kenway, G. K. W., and Martins, J. R. R. A., "Aerodynamic Shape Optimization Investigations of the Common Research Model Wing Benchmark," *AIAA Journal*, Vol. 53, No. 4, April 2015, pp. 968-985.  
doi:10.2514/1.J053318
- [6] Chen, S., Lyu, Z., Kenway, G. K. W., and Martins, J. R. R. A., "Aerodynamic Shape Optimization of the Common Research Model Wing-Body-Tail Configuration," *Journal of Aircraft*, Vol. 53, No. 1, Jan. 2016, pp. 276-293.  
doi:10.2514/1.C033328
- [7] Kenway, G. K. W., and Martins, J. R. R. A., "Multipoint Aerodynamic Shape Optimization Investigations of the Common Research Model Wing," *AIAA Journal*, Vol. 54, No. 1, Jan. 2016, pp. 113-128.  
doi:10.2514/1.J054154
- [8] LeDoux, S. T., Vassberg, J. C., Young, D. P., Fugal, S., Kamenetskiy, D., Huffman, W. P., Melvin, R. G., and Smith, M. F., "Study Based on the AIAA Aerodynamic Design Optimization Discussion Group Test Cases," *AIAA Journal*, Vol. 53, No. 7, Feb. 2015, pp. 1910-1935.  
doi:10.2514/1.J053535
- [9] Vassberg, J., and Jameson, A., "Influence of Shape Parameterization on Aerodynamic Shape Optimization," Tech. Rept., Von Karman Inst., Brussels, April 2014.
- [10] Telidetzki, K., Osusky, L., and Zingg, D. W., "Application of Jetstream to a Suite of Aerodynamic Shape Optimization Problems," *52nd Aerospace Sciences Meeting*, AIAA Paper 2014-0571, Feb. 2014.  
doi:10.2514/6.2014-0571
- [11] Carrier, G., Destarac, D., Dumont, A., Méheut, M., Din, I. S. E., Peter, J., Khelil, S. B., Brezillon, J., and Pestana, M., "Gradient-Based Aerodynamic Optimization with the elsA Software," *52nd Aerospace Sciences Meeting*, AIAA Paper 2014-0568, Feb. 2014.  
doi:10.2514/6.2014-0568
- [12] LeDoux, S. T., Young, D. P., Fugal, S., Elliott, J. K., Kamenetskiy, D. S., Melvin, R. G., and Huffman, W. P., "A Study Based on the AIAA Aerodynamic Design Optimization Discussion Group Test Cases," *53rd AIAA Aerospace Sciences Meeting*, AIAA Paper 2015-1717, Jan. 2015.  
doi:10.2514/6.2015-1717
- [13] Jutte, C. V., Stanford, B. K., Wieseman, C. D., and Moore, J. B., "Aeroelastic Tailoring of the NASA Common Research Model via Novel Material and Structural Configurations," *52nd Aerospace Sciences Meeting*, AIAA Paper 2014-0598, Jan. 2014.  
doi:10.2514/6.2014-0598
- [14] Stanford, B. K., Jutte, C. V., and Wieseman, C. D., "Trim and Structural Optimization of Subsonic Transport Wings Using Nonconventional Aeroelastic Tailoring," *AIAA Journal*, Vol. 54, No. 1, Oct. 2015, pp. 293-309.  
doi:10.2514/1.J054244
- [15] Klimmek, T., "Parametric Set-Up of a Structural Model for FERMAT Configuration Aeroelastic and Loads Analysis," *Journal of Aeroelasticity and Structural Dynamics*, Vol. 3, No. 2, 2014, pp. 31-49.  
doi:10.3293/asdj.2014.27
- [16] Keye, S., Klimmek, T., Abu-Zurayk, M., Schulze, M., and Ilic, C., "Aero-Structural Optimization of the NASA Common Research Model," *18th AIAA/ISSMO Multidisciplinary Analysis and Optimization Conference*, AIAA Paper 2017-4145, June 2017.
- [17] Lyu, Z., Kenway, G. K., Paige, C., and Martins, J. R. R. A., "Automatic Differentiation Adjoint of the Reynolds-Averaged Navier-Stokes Equations with a Turbulence Model," *21st AIAA Computational Fluid Dynamics Conference*, AIAA Paper 2013-2581, July 2013.  
doi:10.2514/6.2013-2581
- [18] Kenway, G. K. W., Kennedy, G. J., and Martins, J. R. R. A., "Aerostructural Optimization of the Common Research Model Configuration," *15th AIAA/ISSMO Multidisciplinary Analysis and Optimization Conference*, AIAA Paper 2014-3274, June 2014.  
doi:10.2514/6.2014-3274
- [19] Burdette, D., Kenway, G. K. W., Lyu, Z., and Martins, J. R. R. A., "Aerostructural Design Optimization of an Adaptive Morphing Trailing Edge Wing," *56th AIAA/ASCE/AHS/ASC Structures, Structural Dynamics, and Materials Conference*, AIAA Paper 2015-1129, Jan. 2015.  
doi:10.2514/6.2015-1129
- [20] Kitson, R. C., Lupp, C., and Cesnik, C. E., "Modeling and Simulation of Flexible Jet Transport Aircraft with High-Aspect-Ratio Wings," *15th Dynamics Specialists Conference*, AIAA SciTech Forum, AIAA Paper 2016-2046, Jan. 2016.
- [21] Brooks, T. R., Kennedy, G. J., and Martins, J. R. R. A., "High-Fidelity Multipoint Aerostructural Optimization of a High Aspect Ratio Tow-Steered Composite Wing," *58th AIAA/ASCE/AHS/ASC Structures, Structural Dynamics, and Materials Conference*, AIAA Paper 2017-1350, Jan. 2017.  
doi:10.2514/6.2017-1350
- [22] Burdette, D. A., Kenway, G. K., and Martins, J. R. R. A., "Performance Evaluation of a Morphing Trailing Edge Using Multipoint Aerostructural Design Optimization," *57th AIAA/ASCE/AHS/ASC Structures, Structural Dynamics, and Materials Conference*, AIAA Paper 2016-0159, Jan. 2016.  
doi:10.2514/6.2016-0159
- [23] Chin, T. W., and Kennedy, G. J., "Large-Scale Compliance-Minimization and Buckling Topology Optimization of the Undeformed Common Research Model Wing," *57th AIAA/ASCE/AHS/ASC Structures, Structural Dynamics, and Materials Conference*, AIAA Paper 2016-0939, 2016.  
doi:10.2514/6.2016-0939
- [24] Kenway, G. K. W., and Martins, J. R. R. A., "Buffet Onset Constraint Formulation for Aerodynamic Shape Optimization," *AIAA Journal*, Vol. 55, No. 6, June 2017, pp. 1930-1947.  
doi:10.2514/1.J055172
- [25] Kenway, G. K. W., Kennedy, G. J., and Martins, J. R. R. A., "Scalable Parallel Approach for High-Fidelity Steady-State Aeroelastic Analysis and Derivative Computations," *AIAA Journal*, Vol. 52, No. 5, May 2014, pp. 935-951.  
doi:10.2514/1.J052255
- [26] Kennedy, G. J., and Martins, J. R. R. A., "A Parallel Aerostructural Optimization Framework for Aircraft Design Studies," *Structural and Multidisciplinary Optimization*, Vol. 50, No. 6, Dec. 2014, pp. 1079-1101.  
doi:10.1007/s00158-014-1108-9
- [27] Kenway, G. K. W., and Martins, J. R. R. A., "Multipoint High-Fidelity Aerostructural Optimization of a Transport Aircraft Configuration," *Journal of Aircraft*, Vol. 51, No. 1, Jan. 2014, pp. 144-160.  
doi:10.2514/1.C032150
- [28] Liem, R. P., Kenway, G. K. W., and Martins, J. R. R. A., "Multimission Aircraft Fuel Burn Minimization via Multipoint Aerostructural Optimization," *AIAA Journal*, Vol. 53, No. 1, Jan. 2015, pp. 104-122.  
doi:10.2514/1.J052940
- [29] Mader, C. A., Kenway, G., and Martins, J. R. R. A., "Towards High-Fidelity Aerostructural Optimization Using a Coupled ADjoint Approach," *12th AIAA/ISSMO Multidisciplinary Analysis and Optimization Conference*, AIAA Paper 2008-5968, Sept. 2008.
- [30] Kennedy, G. J., and Martins, J. R. R. A., "A Parallel Finite-Element Framework for Large-Scale Gradient-Based Design Optimization of High-Performance Structures," *Finite Elements in Analysis and Design*, Vol. 87, Sept. 2014, pp. 56-73.  
doi:10.1016/j.finel.2014.04.011
- [31] Uyttersprot, L., "Inverse Distance Weighting Mesh Deformation," Ph.D. Thesis, Delft Univ. of Technology, Delft, The Netherlands, 2014.
- [32] Brown, S. A., "Displacement Extrapolation for CFD + CSM Aeroelastic Analysis," *38th Structures, Structural Dynamics, and Materials Conference*, AIAA Paper 1997-1090, 1997.

- [33] Gill, P. E., Murray, W., and Saunders, M. A., "SNOPT: An SQP Algorithm for Large-Scale Constrained Optimization," *SIAM Journal on Optimization*, Vol. 12, No. 4, 2002, pp. 979–1006.
- [34] Perez, R. E., Jansen, P. W., and Martins, J. R. R. A., "pyOpt: A Python-Based Object-Oriented Framework for Nonlinear Constrained Optimization," *Structural and Multidisciplinary Optimization*, Vol. 45, No. 1, Jan. 2012, pp. 101–118.  
doi:10.1007/s00158-011-0666-3
- [35] Vassberg, J., "A Unified Baseline Grid about the Common Research Model Wing/Body for the Fifth AIAA CFD Drag Prediction Workshop (Invited)," *29th AIAA Applied Aerodynamics Conference*, AIAA Paper 2011-3508, June 2011.  
doi:10.2514/6.2011-3508
- [36] "777-200/300 Airplane Characteristics for Airport Planning," Tech. Rept. D6-58329, Boeing Commercial Airplanes, Seattle, WA, July 1998.
- [37] Kennedy, G. J., Kenway, G. K. W., and Martins, J. R. R. A., "High Aspect Ratio Wing Design: Optimal Aerostructural Tradeoffs for the Next Generation of Materials," *52nd Aerospace Sciences Meeting*, AIAA Paper 2014-0596, Jan. 2014.  
doi:10.2514/6.2014-0596
- [38] Akgün, M. A., Haftka, R. T., Wu, K. C., Walsh, J. L., and Garcelon, J. H., "Efficient Structural Optimization for Multiple Load Cases Using Adjoint Sensitivities," *AIAA Journal*, Vol. 39, No. 3, 2001, pp. 511–516.  
doi:10.2514/3.14760
- [39] Lambe, A. B., Martins, J. R. R. A., and Kennedy, G. J., "An Evaluation of Constraint Aggregation Strategies for Wing Box Mass Minimization," *Structural and Multidisciplinary Optimization*, Vol. 55, No. 1, Jan. 2017, pp. 257–277.  
doi:10.1007/s00158-016-1495-1
- [40] Stanford, B. K., and Jutte, C. V., "Comparison of Curvilinear Stiffeners and Tow Steered Composites for Aeroelastic Tailoring of Aircraft Wings," *Computers & Structures*, Vol. 183, April 2017, pp. 48–60.  
doi:10.1016/j.compstruc.2017.01.010
- [41] Bucalem, M. L., and Bathe, K.-J., "Higher-Order MITC General Shell Elements," *International Journal for Numerical Methods in Engineering*, Vol. 36, No. 21, 1993, pp. 3729–3754.  
doi:10.1002/(ISSN)1097-0207
- [42] Kenway, G. W. K., and Martins, J. R. R. A., "High-Fidelity Aerostructural Optimization Considering Buffet Onset," *16th AIAA/ISSMO Multidisciplinary Analysis and Optimization Conference*, AIAA Paper 2015-2790, June 2015.

D. E. Raveh  
Associate Editor